

## Article

# Petrogenesis of Eocene Lamprophyre Dykes in Northern Qiangtang Terrane, Tibetan Plateau: Implications for the Tethyan Mantle Metasomatism and Tectonic Evolution

Xiaohui Zeng<sup>1</sup>, Tingting Gong<sup>1,\*</sup>, Han Zhao<sup>1</sup> and Fuhao Xiong<sup>1,2</sup> 

<sup>1</sup> College of Earth Science, Chengdu University of Technology, Chengdu 610059, China; zengxh22@163.com (X.Z.); zhaohan2013@cdut.edu.cn (H.Z.); fhxiong@cdut.edu.cn (F.X.)

<sup>2</sup> State Key Laboratory of Oil and Gas Reservoir Geology and Exploitation, Chengdu University of Technology, Chengdu 610059, China

\* Correspondence: gongtingting2013@cdut.edu.cn

**Abstract:** Post-collisional (ultra)potassic lamprophyre dykes are the key probes for understanding mantle metasomatism and reconstructing tectonic evolution. In this study, we present new petrological, geochronological, geochemical and zircon Lu-Hf isotopic data for lamprophyre dykes in the northern Qiangtang terrane (central Tibet), aiming to constrain their petrogenesis and geodynamic setting. The studied lamprophyres are minettes with phenocrysts of siderophyllite and phlogopite, which intrude into Triassic granite of 236.9 Ma. These lamprophyres yield zircon U-Pb ages of 39.7–40.9 Ma. They exhibit high contents of K<sub>2</sub>O (7.61–8.59 wt.%) and ultrapotassic features with high K<sub>2</sub>O/Na<sub>2</sub>O (11.43–14.38) ratios. They are characterized by increased values of Mg# (69.1 to 72.1) and high concentrations of compatible elements (e.g., Cr = 277–529 ppm, Ni = 232–322 ppm), which are diagnostic of mantle-derived primitive magma. The studied lamprophyres have a high abundance of rare earth elements ( $\Sigma$ REE = 902–1061 ppm) with significantly fractionated REE patterns ((La/Yb)<sub>N</sub> = 66.3–100.6), and they are enriched in large ion lithophile elements (LILE) and light rare earth elements (LREE), but depleted in high field strength elements (HFSE) (e.g., Nb, Ta and Ti) and heavy rare earth elements (HREE) with enriched zircon Hf isotopes ( $\epsilon$ Hf(t) from –6.40 to 3.80). This indicates their derivation from an enriched mantle source which was metasomatized by subduction-related fluids and sediment-derived melts. A petrogenetic study suggests that the lamprophyres were generated by the partial melting of a phlogopite-bearing lherzolite within the garnet stability field. We propose that the Cenozoic ultrapotassic mafic rocks in the central Tibetan Plateau originated in the lithospheric mantle metasomatized by the subduction-related components, and are the magmatic response to the detachment of the subducted Tethyan slab.

**Keywords:** lamprophyre; ultrapotassic magma; Tethys orogeny; northern Qiangtang



**Citation:** Zeng, X.; Gong, T.; Zhao, H.; Xiong, F. Petrogenesis of Eocene Lamprophyre Dykes in Northern Qiangtang Terrane, Tibetan Plateau: Implications for the Tethyan Mantle Metasomatism and Tectonic Evolution. *Minerals* **2023**, *13*, 1349. <https://doi.org/10.3390/min13101349>

Academic Editor: Ioan Seghedi

Received: 4 September 2023

Revised: 18 October 2023

Accepted: 18 October 2023

Published: 23 October 2023



**Copyright:** © 2023 by the authors. Licensee MDPI, Basel, Switzerland. This article is an open access article distributed under the terms and conditions of the Creative Commons Attribution (CC BY) license (<https://creativecommons.org/licenses/by/4.0/>).

## 1. Introduction

Post-collisional potassic–ultrapotassic magmatic rocks are key probes for unveiling the magmatic–tectonic evolution of intracontinental orogenic stages [1,2]. Their petrogenesis is of great significance for understanding the growth and evolutionary mechanism of the lithosphere as well as the associated geodynamic processes. Large-scale Cenozoic potassic–ultrapotassic magmatic rocks occur in the central Tibetan Plateau, which record the magmatic–tectonic evolution of the region during the Neo-Tethys orogeny [3,4]. Large numbers of petrological, geochronological and geochemical studies have been carried out on Cenozoic potassic–ultrapotassic magmatic rocks in the central Tibetan Plateau to understand the magmatic ages, petrogenesis and tectonic settings [5,6]. However, the geodynamics of the potassic–ultrapotassic magmatic rocks in this area are still controversial [5,7–9]. Several models have been proposed including slab break-off [3,10–12], convective removal

or delamination of the lower lithosphere [7,13,14] or intracontinental subduction [15]. Moreover, although previous studies have suggested that the potassic–ultrapotassic magmatic rocks in this area are derived from subducting continental lithosphere [10,16], partial melting of the lithospheric mantle has also been proposed to contribute to their genesis [15]. Previous studies mainly focused on intermediate–felsic potassic–ultrapotassic rocks rather than mantle-derived mafic ones [3,4,15–17]. This severely impeded our understanding of the mantle properties, potassium enrichment mechanism and associated geodynamic process of Cenozoic potassic–ultrapotassic magmatism in the central Tibetan Plateau.

As mantle-derived mafic–ultramafic igneous rocks, lamprophyres are characterized by hydrous mafic silicates (hornblende and/or mica) and small sizes [18]. According to the International Union of Geological Sciences (IUGS) classification criteria [19], lamprophyres can be divided into ultramafic, calc-alkaline and alkaline. Among them, the ultramafic lamprophyres are often the magmatic product of lithospheric extension, rift-related and continental rupture areas, and usually form dyke swarms associated with carbonatite rocks [20]. Calc-alkaline lamprophyres usually develop in convergent or passive continental margins and are often associated with shoshonite or calc-alkaline magmatic rocks, which are important indicators of crust–mantle interactions [21,22]. Alkaline ones are mostly exposed in discrete plate margin (continental rift) or continental plate (mantle plume-related) environments, which are closely related to intraplate alkaline basaltic magmatism [23]. Thus, lamprophyres can be used as key probes for understanding the properties of the lithospheric mantle and regional tectonic evolution. Due to their high contents of hydrous mafic minerals, lamprophyres are generally considered to be derived from enriched mantle [24–26]. However, the enrichment mechanisms for the mantle sources remain enigmatic. There are several different models, including metasomatism induced by slab-derived fluids and/or melts [27–29] and metasomatism induced by fluids and/or melts from the deep asthenosphere and/or mantle media [30]. Particularly for the (ultra)potassic lamprophyres, the potassium-enrichment mechanism is actually controlled by its dynamic mechanism, which is, however, poorly understood and restricts our understanding of the genetic background of Cenozoic potassic–ultrapotassic magmatism in the Tibetan Plateau. The newly discovered Cenozoic lamprophyres in this area show ultrapotassic characteristics, providing an ideal object for exploring the enrichment mechanism of the lithospheric mantle. This study presents petrological, geochronological, geochemical and Hf isotopic studies on the Rumei lamprophyres, aiming to reveal their petrogenesis and geodynamic implications for the Tethyan orogeny in central Tibet.

## 2. Regional Geology

The Qiangtang Block located on the central Tibetan Plateau is bounded by the Jinshajiang suture to the north and by the Bangong-Nujiang suture to the south (Figure 1a). The two sutures represent the remnants of the Palaeo-Tethyan Ocean and Mid-Tethyan Ocean, respectively. The Longmu Co-Shuanghu-Lancang Suture [31] is a 500 km-long metamorphic belt that mainly consists of ophiolitic mélanges of Cambrian to Triassic [32] and Permian to Triassic high pressure-low temperature metamorphic rocks [33,34]. It was identified and proposed to be a structure dividing the Qiangtang terrane into northern and southern Qiangtang and marking the boundary between Gondwana and Laurasia in the central Qiangtang [31,32].

Eocene magmatic rocks are widespread across the Tibetan Plateau (Figure 1a). In the Qiangtang terrane, these rocks consist of sodic series [35] and high-K calc-alkaline to shoshonite series [10,19,20]. The sodic series rocks are mainly found within the Bangdaco area in the Northern Qiangtang terrane and have ages ranging from 60 to 45 Ma [35]. The high-K calc-alkaline to shoshonite series rocks are mainly found within the Duogecuoren area (45–37 Ma) and Yulong area (51–37 Ma) in the Northern Qiangtang terrane [10,19,20], with minor occurrences in the Nadingco area (34 Ma) in the Southern Qiangtang terrane near the Bangong-Nujiang suture zone [36].

The Rumei area, located in the east of the Northern Qiangtang terrane, ca. 330 km southeast of Nangqen City (Figure 1a), is the turning area of the east-west tectonic belt of the Tibetan Plateau to the north-south tectonic belt of the Hengduan Mountains. The studied lamprophyres are located about 5 km northwest of Rumei Township and occur as NW trending dykes, which mainly intrude into the Middle–Late Triassic volcanic-sedimentary strata (Figure 1b). They are consistent with the trend of regional structure (Figure 1b).

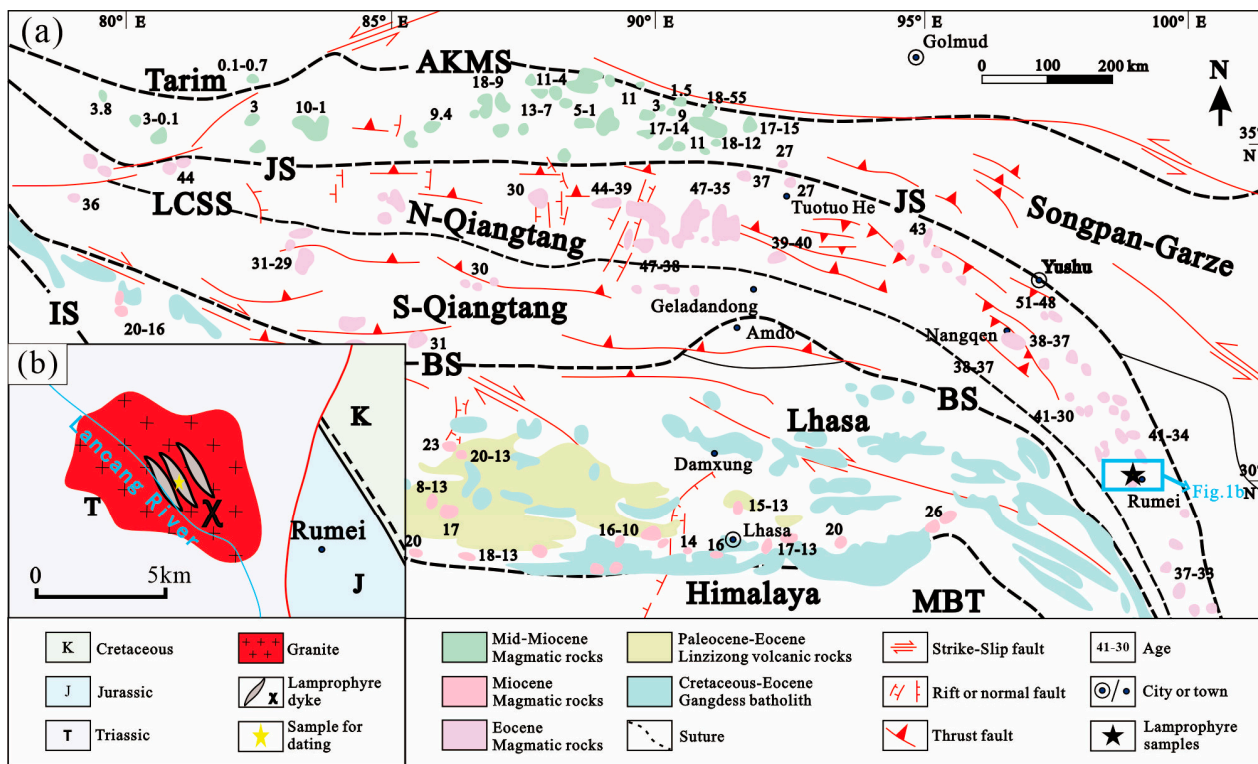
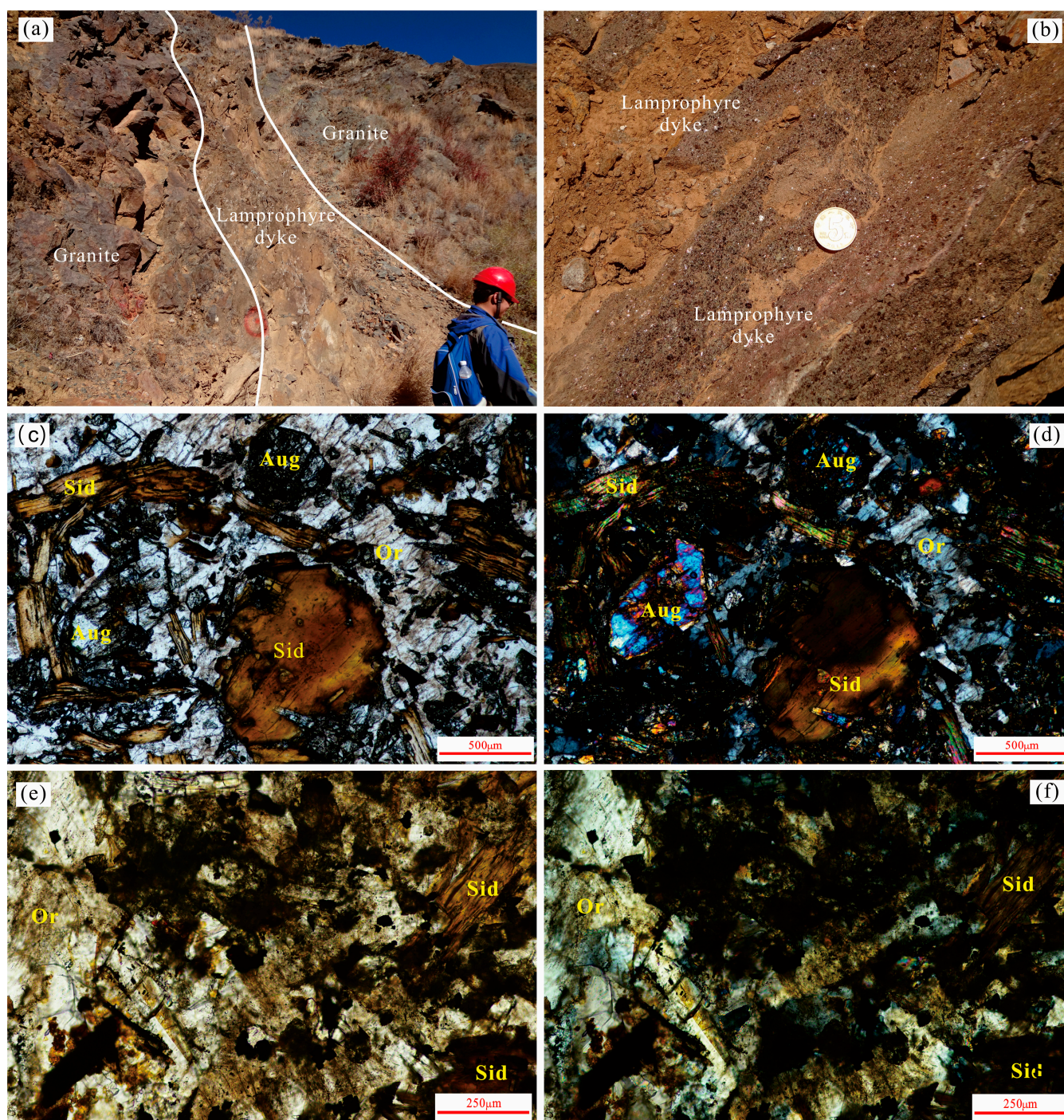


Figure 1. (a) Map of the Tibetan Plateau showing major continental blocks and the temporal-spatial distribution of Cenozoic igneous rocks (modified from [37,38]). Main suture zones between major blocks: IS = Indus; BS = Bangong; LCSS = Longmuco–Shuanghu; JS = Jinshajiang; AKMS = Anyimaqen–Kunlun–Muztagh. Major faults: MBT = Main Boundary Thrust. (b) Geological map of the Rumei area in the Northern Qiangtang terrane.

### 3. Petrology and Petrography

The Rumei lamprophyres occur as NW-trending dykes intruding into Triassic granite (Figure 2a,b). The sampled lamprophyres are minettes (based on the classification scheme [24]), and display predominantly porphyritic textures (Figure 2a–f). The main phenocrysts are composed of euhedral-subhedral siderophyllite (20%–30%), phlogopite (2%–10%) and augite (5%–10%), whereas the matrix consists of subhedral-anhedral orthoclase (~30%), augite (~5%) and siderophyllite (~12%) (Figure 2c–f). Accessory minerals, such as Fe–Ti oxides, apatite and zircon, have also been identified in the matrix. Augite, siderophyllite and phlogopite phenocrysts in these minettes are altered to varying degrees, while some orthoclase grains are moderately to severely altered to chlorite, epidote, illite and other minerals. Secondary minerals are mainly carbonates and chlorite. According to the mineralogical classification and nomenclature of lamprophyres recommended by IUGS [19], combined with the modal abundance of pyroxene, mica and plagioclase, the Rumei lamprophyres can be classified as pyroxene minette.



**Figure 2.** Field photographs showing representative outcrops (a,b) and photomicrographs of representative samples of the lamprophyres (c–f). Abbreviations are as follows: Sid—siderophyllite, Aug—augite, Or—orthoclase.

#### 4. Analytical Methods

##### 4.1. Zircon U-Pb Geochronology

U-Pb dating and trace element analysis of zircon were simultaneously conducted using LA-ICP-MS at Sample Solution Analytical Technology Co., Ltd., Wuhan, China. The detailed operating conditions for the laser ablation system, the ICP-MS instrument and data reduction are the same as in [39]. Laser sampling was carried out using a GeolasPro laser ablation system, which included a COMPexPro 102 ArF excimer laser (193 nm wavelength,

maximum energy of 200 mJ), and a MicroLas optical system. An Agilent 7900 ICP-MS instrument was used to measure ion-signal intensities. Zircon 91500 and glass NIST610 were utilized as external standards for U-Pb dating and trace element calibration [40], respectively. Each analysis involved approximately 20–30 s of background acquisition followed by 50 s of data acquisition from the sample. ICPMSDataCal 11.8, an Excel-based software, was employed for off-line selection and integration of background and analyzed signals, time-drift correction, and quantitative calibration for trace element analysis and U-Pb dating [41,42]. Concordia diagrams and weighted-mean calculations were generated using Isoplot [43].

#### 4.2. Whole-Rock Geochemistry

Samples for whole-rock geochemical analysis were ground to <200 mesh in an agate ring mill. The analysis of major elements and trace elements was completed at Sample Solution Analytical Technology Co., Ltd., Wuhan, China. Major-element analyses were measured by XRF (Primus II, Rigaku, Japan) using a fused glass disk. The sample pretreatment for whole-rock major-element analysis was performed using the melting method. The flux was a mixture of lithium tetraborate, lithium metaborate and lithium fluoride (45:10:5). Ammonium nitrate and lithium bromide were used as the oxidant and release agent, respectively. The melting temperature was 1050 °C and the melting time was 15 min. Samples for trace-element analysis were digested by HF+HNO<sub>3</sub> in Teflon crucibles and analyzed using an Agilent 7700e ICP-MS. The accuracy was better than 5%–10%. The detailed sample digestion procedure is the same as that described in [42].

#### 4.3. Zircon Lu-Hf Isotopes

In situ Hf isotope analyses of zircon were conducted using a Neptune Plus MC-ICP-MS (Thermo Fisher Scientific, Bremen, Germany) in combination with a Geolas HD laser ablation system (Coherent, Göttingen, Germany) at Sample Solution Analytical Technology Co., Ltd., Wuhan, China. All data were acquired in single-spot ablation mode at a spot size of 44 µm. Each measurement consisted of 20 s of acquisition of the background signal followed by 50 s of ablation. Off-line selection and integration of analytical signals were performed using ICPMSDataCal [41]. Zircon standards 91500 and GJ-1 were used to check instrument reliability and stability [40]. The detailed operating conditions for the laser ablation system, the MC-ICP-MS instrument and analytical method are the same as described in [44].

## 5. Results

### 5.1. Major Elements

Major-element concentrations are shown in Supplementary Table S1. The Rumei lamprophyre samples have low contents of SiO<sub>2</sub> (44.15–49.06 wt.%). In the (Na<sub>2</sub>O+K<sub>2</sub>O) vs. SiO<sub>2</sub> diagram, most samples plot in the tephrite and phonotephrite fields, and only one plots in the feldspathoid field and belongs to the alkaline series (Figure 3a,b). These samples show low contents of Na<sub>2</sub>O (0.53–0.69 wt.%), medium contents of P<sub>2</sub>O<sub>5</sub> (1.69–1.89 wt.%), TiO<sub>2</sub> (0.69–1.90 wt.%) and Fe<sub>2</sub>O<sub>3</sub> (6.31–7.23 wt.%), and high contents of K<sub>2</sub>O (7.61–8.59 wt.%) and MgO (7.36–9.34 wt.%) with high K<sub>2</sub>O/Na<sub>2</sub>O (11.43–14.38) and Mg# (69.1–72.1). In the SiO<sub>2</sub> vs. K<sub>2</sub>O diagram (Figure 3c), they fall in the field of lamproites. The lamprophyres with relatively high K<sub>2</sub>O/Na<sub>2</sub>O ratios can also be ultrapotassic (Figure 3d). The major-element concentrations were normalized to 100% on an anhydrous basis in all diagrams.

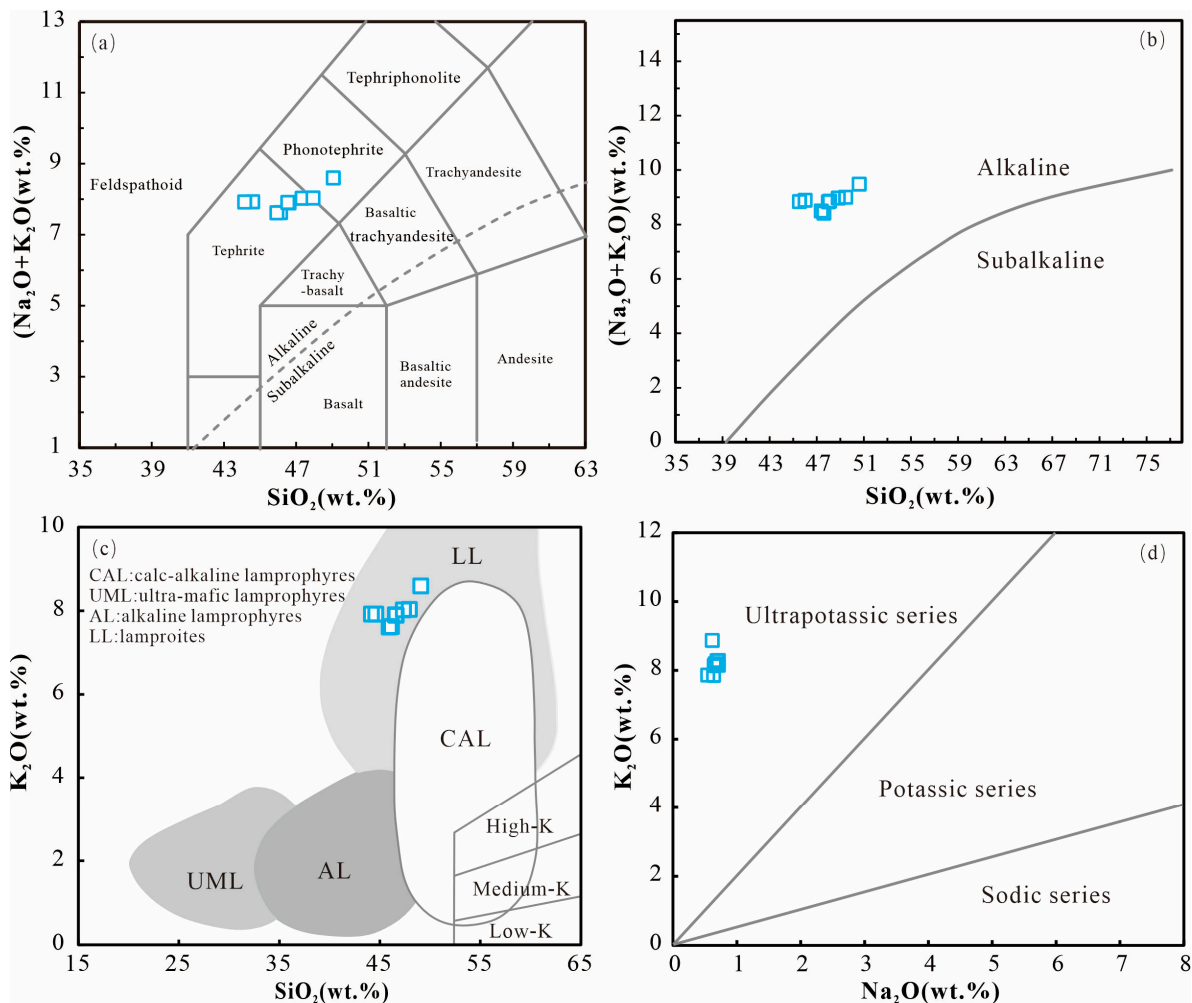


**Figure 3.** Geochemical classification of lamprophyres from the Rumei area. (a) Total alkali vs. silica (TAS) diagram [45]; (b)  $K_2O+Na_2O$  vs.  $SiO_2$  diagram [46]; (c)  $K_2O$  vs.  $SiO_2$  diagram [47]; (d)  $K_2O$  vs.  $Na_2O$  diagram [19].

### 5.2. Rare Earth Elements

Rare earth element concentrations are shown in Supplementary Table S1. The total REE contents of the lamprophyres range from 902 ppm to 1061 ppm (average 949 ppm). These samples are enriched in LREE and show high LREE/HREE fractionation ( $(La/Yb)_N = 66.3\text{--}100.6$ ) (Figure 4). The normalized REE distribution patterns are similar to the typical coeval potassic–ultrapotassic rocks of the Qiangtang terrane [3,4,47]. The samples from the Rumei area have slightly negative Eu anomalies ( $Eu/Eu^* = 0.81\text{--}0.86$ ).

### 5.3. Trace Elements

Trace-element concentrations are shown in Supplementary Table S1. On the primitive mantle-normalized diagram (Figure 5), the lamprophyres show enrichment in the fluid mobile large ion lithophile elements (LILEs)—Rb, Ba and K. There is a depletion in Nb, Ta and Ti (high field strength elements). The Pb–Sr composition of lamprophyres shows a slight enrichment.

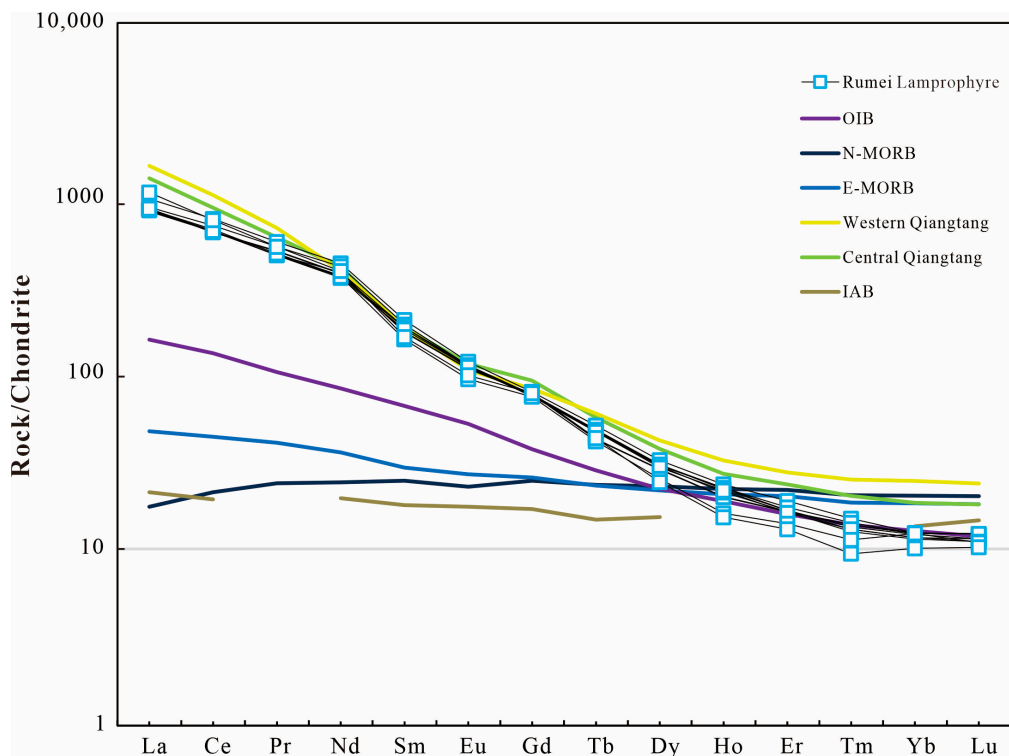


**Figure 4.** Chondrite-normalized REE patterns for samples from the Rumei lamprophyres. Normalizing and OIB values are from [48], E-MORB from [49], N-MORB from [50], IAB from [51], regional data on typical ultrapotassic rocks in the Western Qiangtang terrane come from [3] and in the Central Qiangtang terrane from [52].

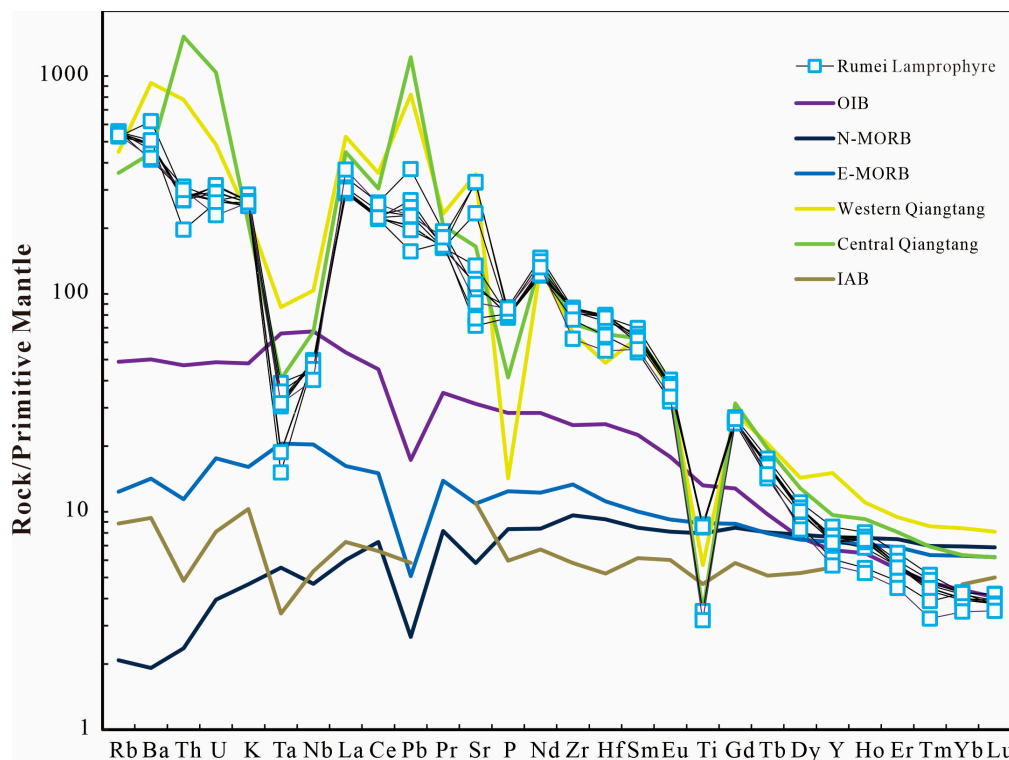


**Figure 5.** Primitive mantle-normalized trace element patterns for Rumei lamprophyres. The data sources are the same as in Figure 4.

#### 5.4. LA-ICP-MS Zircon U-Pb Isotopic Data

The zircon U-Pb isotopic data and calculated ages are listed in Supplementary Table S2. Most analyzed zircons are euhedral to subhedral, prismatic and transparent with crystal lengths ranging from 70 to 120  $\mu\text{m}$ . The zircons from two lamprophyre samples (G14B2-1, G14B2-2) and one granite (D03B1) sample were analyzed, which all had identical oscillatory zoning in CL images (Figure 6a,c,e).

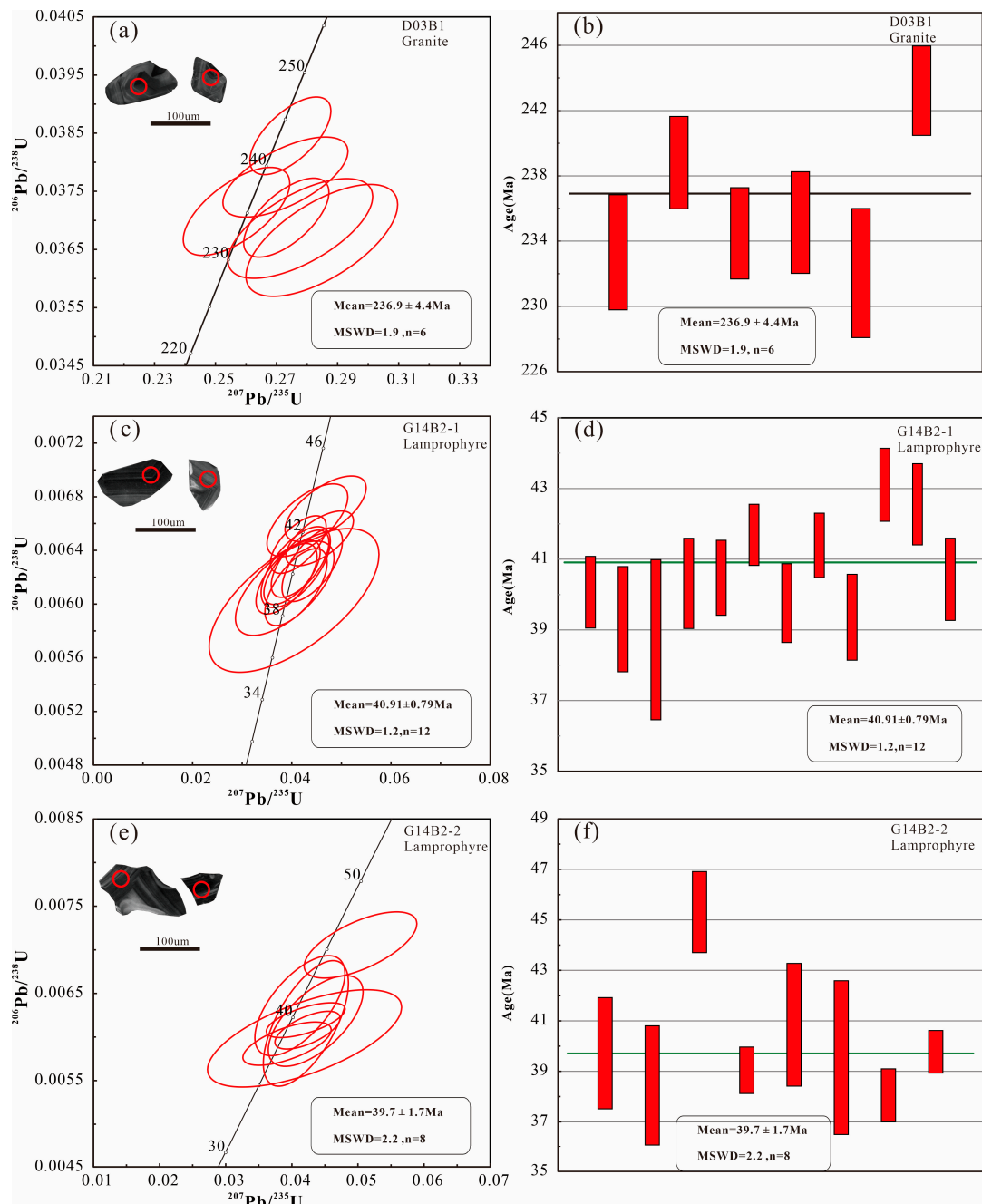


**Figure 6.** LA-ICP-MS zircon U-Pb concordia diagrams (a,c,e), weighted-mean  $^{206}\text{Pb}/^{238}\text{U}$  age (b,d,f) and representative cathodoluminescence images (a,c,e) of zircon for granite (D03B1) and lamprophyre dykes (G14B2-1 and G14B2-2) from the Rumei area.

A total of twenty zircon U-Pb isotope analyses were obtained from granite (Supplementary Table S2). These grains exhibited variably high contents of Th (378–3885 ppm) and U (604–3714 ppm), with high Th/U ratios (0.44–1.27). The apparent  $^{206}\text{Pb}/^{238}\text{U}$  ages

correspond to 232.1–243.3 Ma with a weighted mean of  $236.9 \pm 4.4$  Ma (MSWD = 1.9,  $n = 6$ ; Figure 6a,b). This value is interpreted as the crystallization age of the host granite.

Twenty zircon grains from lamprophyre G14B2-1 were analyzed, and they were found to have high contents of Th (278–5672 ppm) and U (1091–3115 ppm), and high Th/U ratios (0.20–2.07). The  $^{206}\text{Pb}/^{238}\text{U}$  ages correspond to 38.74–43.11 Ma, yielding a weighted mean of  $40.9 \pm 0.79$  Ma (MSWD = 1.2,  $n = 12$ ; Figure 6c,d). A total of twenty analyses have been obtained from lamprophyre G14B2-2, which show variable contents of Th (4–3503 ppm) and U (457–1567 ppm), and high Th/U ratios (0.01–2.27, average 1.3). The apparent  $^{206}\text{Pb}/^{238}\text{U}$  ages correspond to 38.07–45.32 Ma, with a weighted mean of  $39.7 \pm 1.7$  Ma (MSWD = 2.2,  $n = 8$ ; Figure 6e,f). These values are interpreted as the crystallization age of the Rumei lamprophyres.

### 5.5. Zircon Lu-Hf Isotopes

The  $^{176}\text{Yb}/^{177}\text{Hf}$  ratios in the investigated zircons range from 0.000339 to 0.039999, and the  $^{176}\text{Lu}/^{177}\text{Hf}$  ratios range from 0.000010 to 0.001601, suggesting an insignificant accumulation of radiogenic Hf after zircon crystallization [53]. Therefore, the  $^{176}\text{Hf}/^{177}\text{Hf}$  ratios in the magmatic zircons could represent the Hf isotopic compositions of their parental magma. Zircon grains from the Rumei lamprophyres yielded  $^{176}\text{Hf}/^{177}\text{Hf}$  isotopic ratios ranging from 0.282566 to 0.282854 with  $\epsilon\text{Hf}(t)$  values from  $-6.40$  to  $3.80$ . The crustal model ages ( $T_{\text{DM}2}$ ) varied from 0.88 to 1.53 Ga (Figure 7; Supplementary Table S3).

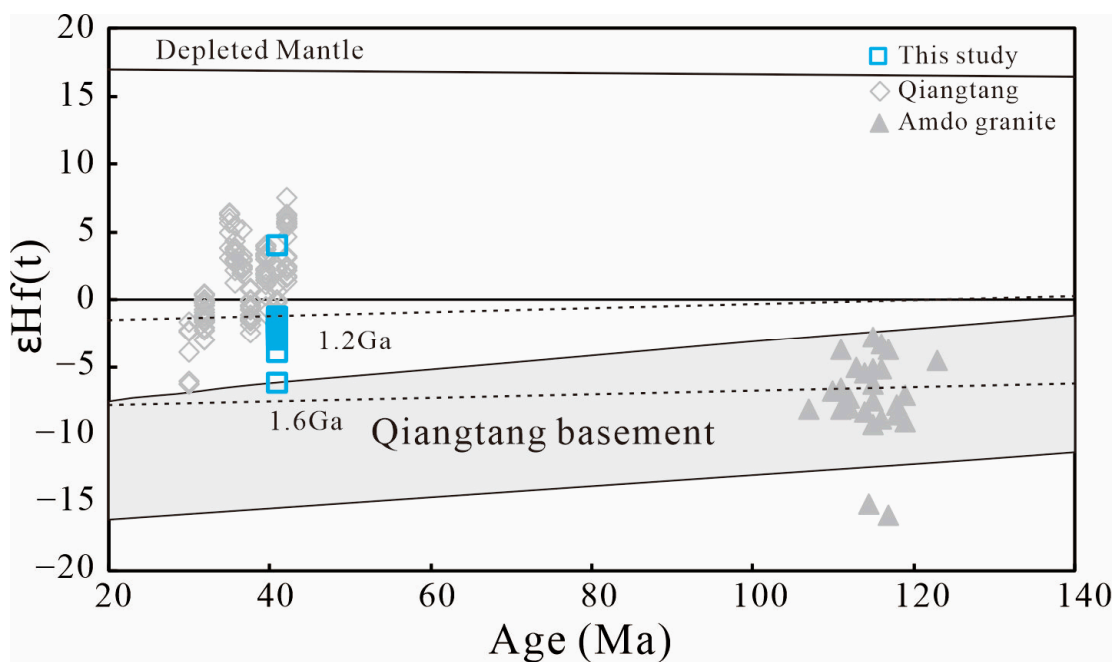


**Figure 7.** Correlation of zircon  $\epsilon\text{Hf}(t)$  values vs. zircon U-Pb ages [54] for the lamprophyre dykes in the Rumei area, Northern Qiangtang terrane. The data from Qiangtang correspond to (ultra)potassic rocks [36,55–60]. The data for Amdo granite and Qiangtang basement are from [61].

## 6. Discussion

### 6.1. Petrogenesis of the Rumei Lamprophyre

#### 6.1.1. Effects of Post-Magmatic Alterations

It is necessary to evaluate the effects of the post-magmatic alterations on the lamprophyre dykes, as most of the samples have relatively high loss-on-ignition values (LOI; 1.91–6.36 wt.%). Besides containing a large amount of water-rich minerals such as siderophyllite, mineral alteration will also affect the LOI. The petrography of the lamprophyres revealed different degrees of alteration of the primary minerals, modified by chloritization,

epidote and illitization. Moreover, the slightly enriched Pb-Sr components also indicated that the sample was affected by alteration.

#### 6.1.2. Crustal Contamination

Before constraining the magma source characteristics of the lamprophyre dykes, it is necessary to assess the possible influences of the crustal contamination. However, the following characteristics suggest that the lamprophyres did not undergo significant shallow-level crustal contamination: (1) high concentrations of MgO (7.36–9.34 wt.%), Ni (232–322 ppm) and Cr (277–529 ppm); (2) relatively primitive characteristics, as demonstrated by their Mg# (69.1 to 72.1, average 70.3), and the absence of cumulate textures indicating that the parental magma was derived from partial melting of the mantle (Figure 8d); (3) higher concentrations of Rb, Sr and Th in the samples compared to upper- and lower-crustal rocks [62]; and (4) negative Ta, Nb and Ti anomalies (Figure 5).

#### 6.1.3. Magma Source

The Rumei lamprophyres have a high K<sub>2</sub>O content and significant LILE enrichment, indicating a LILE-enriched mantle source. Amdo granite originated from rock melting in the Qiangtang block basement, and its isotopic composition can represent the continental crust basement [62]. Therefore, we selected Amdo granite, and carried out isotopic calculations with reference to the Cenozoic era; the results indicated that the lamprophyres originated from enriched mantle (Figure 7). Because all REE are strongly incompatible in spinel, and HREE are preferentially partitioned into garnet [63], the high ratios of La/Sm (7.11–10.3), Sm/Yb (11.5–15.0) and (Tb/Yb)<sub>N</sub> (3.35–4.25) in the lamprophyres imply their derivation from the relatively deep garnet-bearing mantle at high pressure (Figure 8a,b). Volatile-bearing minerals such as phlogopite and amphibole are the major hosts for LILEs in the lithospheric mantle [64]. As Rb and Ba are compatible with phlogopite structures [65], and Rb, Sr and Ba are moderately compatible with amphibole [66], melts in equilibrium with amphibole are expected to have significantly lower Rb/Sr ratios (<0.1) and higher Ba/Rb ratios (>20) [67]. In contrast, partial melts from a phlogopite-bearing source may have extremely low Ba and Ba/Rb values [68]. The lamprophyres have higher Rb/Sr (0.05–0.23) and lower Ba/Rb ratios (8.14–12.9), indicating a predominance of phlogopite over amphibole in the partial melting zone (Figure 8c). Combined with the Hf vs. Hf/Yb diagram (Figure 8d), the lamprophyres are thought to have been derived from the phlogopite-bearing garnet lherzolite.

#### 6.1.4. Mechanisms of Mantle Metasomatism

The Rumei lamprophyres display a high concentration of incompatible elements, including K, Rb, Ba, Sr, Th and LREE. These elements, along with the enrichment in Hf isotopes, suggest that extensive metasomatism occurred in the magma source. Mantle fluids can be divided into two types according to their geochemical properties and sources. The first type is related to subducted plates or delaminated continental lithosphere, which is characterized by an enrichment of incompatible elements such as K, Rb, Ba, Th and La and a relative depletion of Nb, Ta and Ti. The other kind of metasomatic agent comes from the asthenosphere or mantle plumes. The fluid composition of it is dominated by CO<sub>2</sub> and/or the melt composition is characterized by a high Nb/Ta ratio [71]. The geochemical characteristics of this agent resemble those of alkaline basalt and lamproite related to oceanic islands. Notably, it is distinguished by enrichment in large ion lithophile elements (LILEs), while Nb, Ta and Ti show no signs of depletion [72].

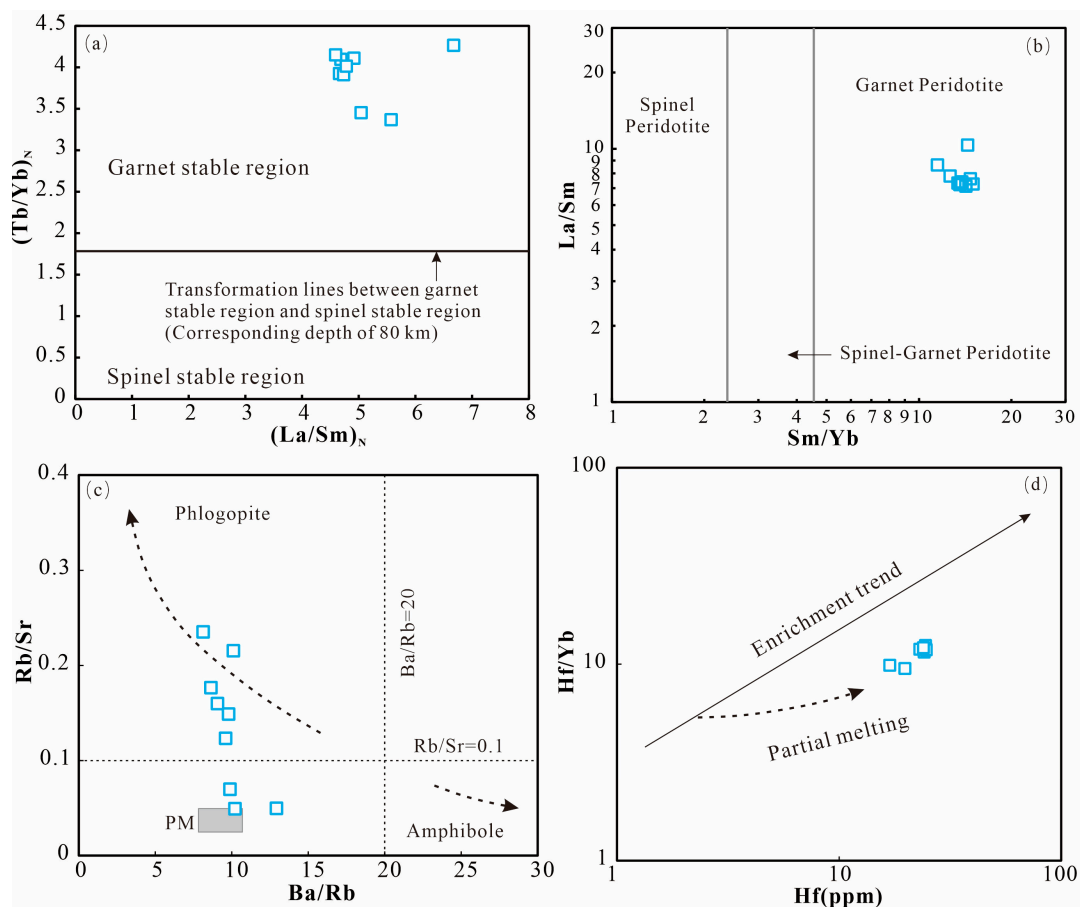


**Figure 8.** (a) The chondrite-normalized  $(La/Sm)_N$  and  $(Tb/Yb)_N$  diagram [69]; (b)  $La/Sm$  vs.  $Sm/Yb$  [29]; (c)  $Rb/Sr$  vs.  $Ba/Rb$  diagram [68]; (d)  $Hf/Hf$  vs.  $Hf/Yb$  diagram [70]. Abbreviation: PM—primitive mantle.

The Rumei lamprophyres are enriched in LILEs and exhibit higher LREE/HREE ratios (26.9–33.8) than those of OIB (Figure 4). Furthermore, they are depleted in HFSEs, especially Nb, Ta and Ti, and the primitive mantle-normalized trace element patterns are distinct from MORB and OIB (Figure 5), but are similar to arc-related volcanic rocks and subduction-zone magmatism. Also, in the  $Th/Yb$  vs.  $Ta/Yb$  diagram, the samples fall in the field of active continental margin (Figure 9a). All of the above indicators demonstrate typical “subduction-related geochemical signatures”.

The dominant metasomatic agents in the subduction zone could be fluids and/or melts from subducted sediments and altered oceanic crust, which are distinguished by the ratios of LILEs, HFSEs and REEs [73]. The partitioning of LILEs, REEs and HFSEs between aqueous fluids and melts is different; therefore, LILEs (such as Rb, Ba, Sr and U) can be transported effectively by fluid phases, whereas REEs and HFSEs are mainly mobilized in the silicate melt [74]. Therefore, mafic magmas with increased  $Rb/Y$  and  $Ba/Yb$  but low  $Nb/Y$ ,  $Nb/Yb$  and  $Ta/Yb$  ratios are commonly interpreted as originating from a mantle source enriched by aqueous fluids. This is also evidenced by the fact that the sample has an imprint of an active continental margin (Figure 9a). Conversely, mafic magmas derived from a mantle source modified by slab-derived melts exhibit the opposite characteristics [72–74]. The studied lamprophyres with high  $Rb/Y$ ,  $Th/Yb$ ,  $Nb/Y$ ,  $Nb/Yb$  and  $Ta/Yb$  are thus thought to be derived from a mantle source modified by both slab melts and aqueous fluids. An enrichment in Ba, Pb and Sr is generally attributed to aqueous fluids, whereas partial melts from subducted sediments are thought to contribute Nb, Th, La, Ce and Nd to the mantle [75]. In the corresponding correlation diagrams (Figure 9b–d), the

lamprophyres exhibit positive correlation trends, reflecting a typical fluid- and melt-related co-enrichment.

The basaltic portion of subducting slabs has relatively low  $K_2O$  and Th contents and Th/La ratios; however, the lamprophyres have high Th contents (16.7–26.4 ppm), indicating that the melt of the metasomatic agent was mainly subducted sediment rather than the basaltic portion. Overall, both subduction-related fluid and sediment-derived melt phases were responsible for the LILE and REE enrichment of the mantle source region.

Based on the experimental data from high-pressure melting of deep-sea sediments and the  $K_2O$ -CaO-MgO-Al<sub>2</sub>O<sub>3</sub>-SiO<sub>2</sub>-H<sub>2</sub>O system, mica (biotite and phengite) has been identified as the only stable hydrous mineral phase capable of carrying large ion lithophile elements (K, Rb, Ba and Cs) to the deep mantle [76]. Subducted sediments tend to have a relatively high content of mica, resulting in an enrichment of potassium (K) in the melts derived from these sediments. The metasomatism of sediment-derived melts and fluids in the subduction zone leads to potassium and water enrichment in the source area. The presence of phlogopite in the source region further suggests that metasomatism of the retained melt occurred prior to mantle melting. Consequently, the partial melting of the phlogopite-bearing mantle sources could then make the magma significantly enriched in K [3].

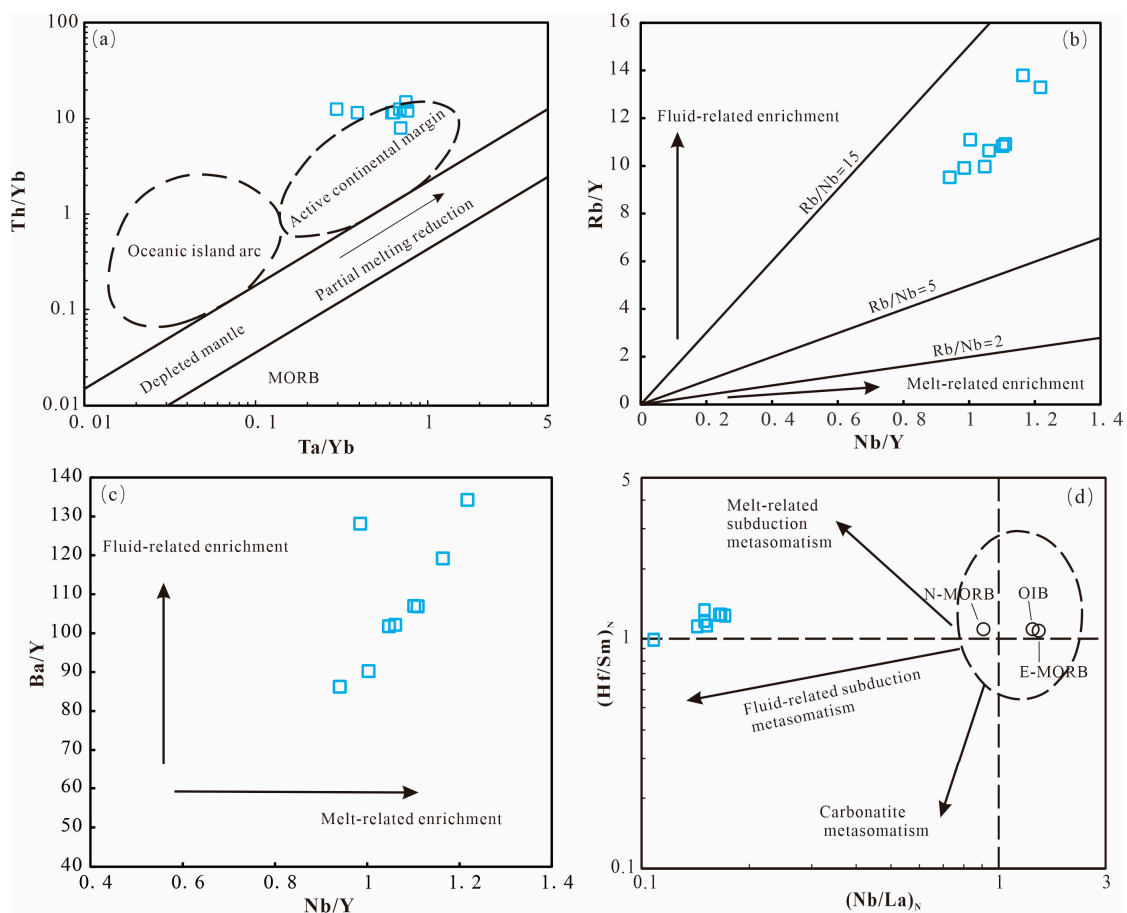


**Figure 9.** Plots of (a) Th/Yb vs. Ta/Yb from [77]; (b) Rb/Y vs. Nb/Y; (c) Ba/Y vs. Nb/Y; (d) Ba vs. Nb/Y, the melt- or fluid-related enrichment trends are from [73,78,79].

## 6.2. Geodynamic Setting

The Tibetan Plateau contains abundant Cenozoic K-rich lavas, which are widely distributed in the main blocks (Lhasa, Qiangtang and Songpan–Ganzi). The potassium-rich magmatic activity began in the Qiangtang block and then migrated to the Lhasa block

and the Songpan–Ganzi block. The widespread Eocene magmatic rocks in the Qiangtang block record the mantle–crust interactions and crustal reworking. Several models have been proposed to explain the petrogenesis of these rocks, which include but are not limited to subduction of oceanic slab and retreat (roll-back) or tearing of the related slab [10], lithospheric delamination/thinning [7], continental lithosphere subduction and related slab retreat or tearing [3,35,80], and partial melting of a mantle plume [81].

As previously discussed, the primitive magmas of the Rumei lamprophyres resulted from low-degree partial melting of the lithospheric mantle, which had undergone metasomatism by subduction-related fluids and sediment-derived melts. These melts and fluids induced metasomatism in the mantle, creating source regions for the K-rich (ultrapotassic or shoshonitic) magmas [82]. During extension, the mantle experienced partial melting, resulting in the formation of ultrapotassic lamprophyres. Different Nb/La ratios indicate distinct tectonic settings. The plots of Nb/La ratios vs. zircon U–Pb ages reveal that the Eocene potassic and ultrapotassic magmatic rocks in the Qiangtang terrane exhibit similar Nb/La ratios (Figure 10). Furthermore, both samples and the regional potassic–ultrapotassic rocks display enriched Hf isotopes (Figure 7). Geographically, the distribution trend of the potassic and ultrapotassic magmatic province in different terranes of central Tibet is roughly parallel to the Himalayas (Figure 1). The linear distribution of these potassic and ultrapotassic rocks suggests a closer association with the India–Asia collision, followed by detachment of the Neo-Tethys oceanic slab from the Indian continental lithosphere at 45 Ma [3,7,16]. This corresponds to the findings of [83], which suggest a north-south extension in northern Tibet during the early Cenozoic.

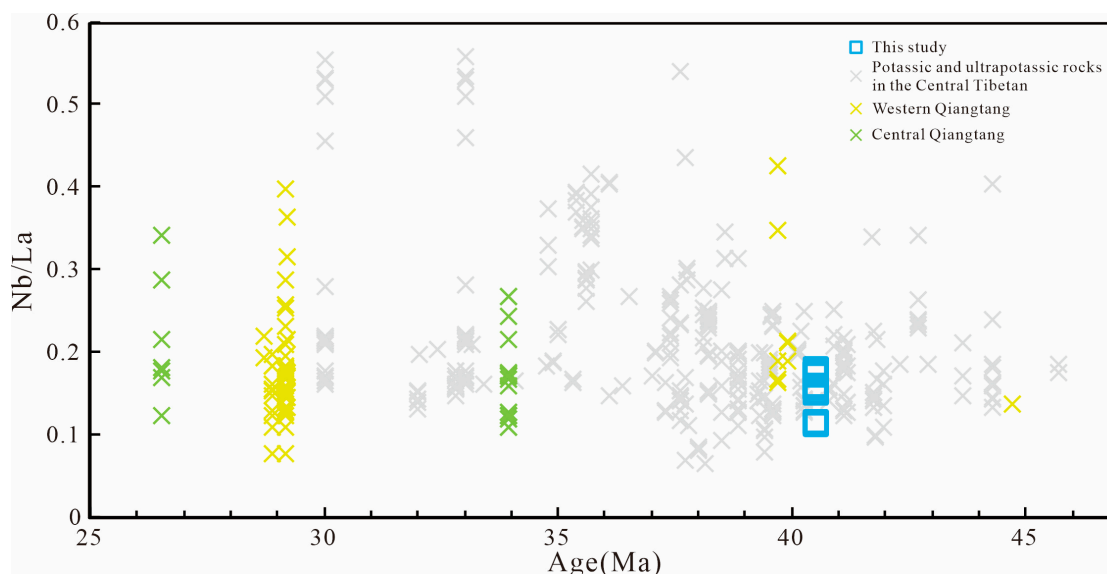


**Figure 10.** Plots of Nb/La vs. zircon U–Pb ages for the Eocene potassic–ultrapotassic rocks in Central Tibet. Data sources are from [3,15–17,35,38,52,56–58,84–86] and references therein.

In summary, the Neo-Tethys oceanic slab broke off during the late Early Eocene. Meanwhile, the upwelling of the asthenosphere also directly contacted the lithospheric mantle to form melts. The primitive magmas were derived from low-degree partial melting of the phlogopite- and garnet-bearing lithospheric mantle. Then, the primitive magmas ascended and formed the potassic–ultrapotassic series rocks in the Qiangtang terrane.

## 7. Conclusions

1. LA-ICP-MS zircon U–Pb dating suggests that the Rumei lamprophyres in the central Tibetan Plateau formed at ca. 39 to 41 Ma.
2. The Rumei lamprophyres are pyroxene minettes, which are strongly enriched in LREE and LILEs, depleted in HREE, Nb, Ta and Ti, and enriched in Hf ( $\epsilon_{\text{Hf}}(t)$  from  $-6.40$  to

- 3.80), indicating that the magma source was partially molten phlogopite-bearing garnet lherzolite.
3. The petrogenetic analyses show that the potassium enrichment of the Rumei lamprophyres was caused by subduction-related fluids and melts metasomatizing the overlying mantle wedge.
  4. The Rumei lamprophyres formed as a response to the Neo-Tethys oceanic slab break-off.

**Supplementary Materials:** The following supporting information can be downloaded at: <https://www.mdpi.com/article/10.3390/min13101349/s1>, Table S1: Whole-rock major and trace element compositions of the studied Eocene Lamprophyre dykes in the Rumei of the northern Qiangtang block; Table S2: LA-ICP-MS zircon U-Pb data for the studied Eocene Lamprophyre dykes in the Rumei of the northern Qiangtang block; Table S3: Zircon Lu-Hf isotopes for the studied Eocene Lamprophyre dykes in the Rumei of the northern Qiangtang block.

**Author Contributions:** Conceptualization, X.Z., T.G. and F.X.; formal analysis, T.G. and H.Z.; resources, F.X.; data curation, F.X.; writing—original draft preparation, X.Z.; writing—review and editing, T.G., H.Z. and F.X. All authors have read and agreed to the published version of the manuscript.

**Funding:** This study was financially supported by the National Natural Science Foundation of China (No. 41602049) and the Research Project of Chengdu University of Technology (No. 2022ZF11412).

**Data Availability Statement:** The original contributions presented in this study are included in the article/Supplementary Material.

**Acknowledgments:** We sincerely thank the journal editors and four anonymous reviewers for their constructive comments and suggestions, which substantially improved our manuscript.

**Conflicts of Interest:** The authors declare no conflict of interest.

## References

1. Zhang, Y.Y.; Guo, Z.J.; Pe-Piper, G.; Piper, D.J.W. Geochemistry and petrogenesis of Early Carboniferous volcanic rocks in East Junggar, North Xinjiang: Implications for post-collisional magmatism and geodynamic process. *Gondwana Res.* **2015**, *28*, 1466–1481. [[CrossRef](#)]
2. Zhu, D.C.; Wang, Q.; Cawood, P.A.; Zhao, Z.D.; Mo, X.X. Raising the Gangdese Mountains in southern Tibet. *J. Geophys. Res. Solid. Earth.* **2017**, *122*, 214–223. [[CrossRef](#)]
3. Guo, Z.F.; Wilson, M.; Liu, J.Q.; Mao, Q. Post-collisional, potassic and ultrapotassic magmatism of the northern Tibetan Plateau: Constraints on characteristics of the mantle source, geodynamic setting and uplift mechanisms. *J. Petrol.* **2006**, *47*, 1177–1220. [[CrossRef](#)]
4. Fan, L.F. Geochemistry of the Cenozoic Bamaoqiongong volcanic rocks in Qiangtang and its tectonic evolution of lithosphere. Master's Thesis, Jilin University, Changchun, China, 2015.
5. Wang, C.S.; Zhao, X.X.; Liu, Z.F.; Lippert, P.C.; Graham, S.A.; Coe, R.S.; Yi, H.S.; Zhu, L.D.; Liu, S.; Li, Y.L. constraints on the early uplift history of the Tibetan Plateau. *Proc. Natl. Acad. Sci. USA* **2008**, *105*, 4987–4992. [[CrossRef](#)] [[PubMed](#)]
6. Ou, Q.; Wang, Q.; Wyman, D.A.; Zhang, C.F.; Hao, L.L.; Dan, W.; Jiang, Z.Q.; Wu, F.Y.; Yang, J.H.; Zhang, H.X. Postcollisional delamination and partial melting of enriched lithospheric mantle: Evidence from Oligocene (ca. 30 Ma) potassium-rich lavas in the Gemuchaka area of the central Qiangtang Block, Tibet. *Geol. Soc. Am. Bull.* **2019**, *131*, 1385–1408. [[CrossRef](#)]
7. Chung, S.L.; Chu, M.F.; Zhang, Y.Q.; Xie, Y.W.; Lo, C.H.; Lee, T.Y.; Lan, C.Y.; Li, X.H.; Zhang, Q.; Wang, Y.Z. Tibetan tectonic evolution inferred from spatial and temporal variations in post-collisional magmatism. *Earth-Sci. Rev.* **2005**, *68*, 173–196. [[CrossRef](#)]
8. Kapp, P.; Decelles, P.G. Mesozoic–Cenozoic geological evolution of the Himalayan-Tibetan orogen and working tectonic hypotheses. *Am. J. Sci.* **2019**, *319*, 159–254. [[CrossRef](#)]
9. Rohrmann, A.; Kapp, P.; Carrapa, B.; Reiners, P.W.; Guynn, J.; Ding, L.; Heizler, M. Thermochronologic evidence for plateau formation in central Tibet by 45 Ma. *Geology* **2012**, *40*, 187–190. [[CrossRef](#)]
10. Prelević, D.; Akal, C.; Foley, S.F.; Romer, R.L.; Stracke, A.; Bogaard, P.V.D. Ultrapotassic Mafic Rocks as Geochemical Proxies for Post-collisional Dynamics of Orogenic Lithospheric Mantle: The Case of Southwestern Anatolia, Turkey. *J. Petrol.* **2012**, *53*, 1019–1055. [[CrossRef](#)]
11. Replumaz, A.; Negrodo, A.M.; Villasenor, A.; Guillot, S. Indian continental subduction and slab break-off during Tertiary collision. *Terra. Nova.* **2010**, *22*, 290–296. [[CrossRef](#)]
12. Zhu, D.C.; Wang, Q.; Zhao, Z.D.; Chung, S.L.; Cawood, P.A.; Niu, Y.; Liu, S.A.; Wu, F.Y.; Mo, X.X. Magmatic record of India-Asia collision. *Sci. Rep.* **2015**, *5*, 14289. [[CrossRef](#)]
13. Kay, R.W.; Kay, S.M. Delamination and delamination magmatism. *Tectonophysics* **1993**, *219*, 177–189. [[CrossRef](#)]

14. Lu, Y.-J.; McCuaig, T.C.; Li, Z.-X.; Jourdan, F.; Hart, C.J.; Hou, Z.-Q.; Tang, S.-H. Paleogene post-collisional lamprophyres in western Yunnan, western Yangtze Craton: Mantle source and tectonic implications. *Lithos* **2015**, *233*, 139–161. [[CrossRef](#)]
15. Zhang, B.; Liu, J.Q.; Chen, W.; Zhu, Z.Y.; Sun, C.Q. Late Eocene magmatism of the eastern Qiangtang block (eastern Tibetan Plateau) and its geodynamic implications. *J. Asian Earth Sci.* **2020**, *195*, 104329. [[CrossRef](#)]
16. Lai, S.C.; Qin, J.F. Adakitic rocks derived from the partial melting of subducted continental crust: Evidence from the Eocene volcanic rocks in the northern Qiangtang block. *Gondwana Res.* **2013**, *23*, 812–824. [[CrossRef](#)]
17. Long, X.P.; Wilde, S.A.; Wang, Q.; Yuan, C.; Wang, X.C.; Li, J.; Jiang, Z.Q.; Dan, W. Partial melting of thickened continental crust in central Tibet: Evidence from geochemistry and geochronology of Eocene adakitic rhyolites in the northern Qiangtang Terrane. *Earth Planet. Sc. Lett.* **2015**, *414*, 30–44. [[CrossRef](#)]
18. Rock, N.M.S. *Lamprophyres*; Blackie Academic & Professional: London, UK, 1991.
19. Le, M.R.W. *Igneous Rocks: A Classification and Glossary of Terms: Recommendations of the International Union of Geological Sciences Subcommission on the Systematics of Igneous Rocks*, 2nd ed.; Cambridge University Press: Cambridge, UK, 2002; pp. 1–236.
20. Pandey, R.; Rao, N.V.C.; Dhote, P.; Pandit, D.; Choudhary, A.K.; Sahoo, S.; Lehmann, B. Rift-associated ultramafic lamprophyre (damtjernite) from the middle part of the Lower Cretaceous (125 Ma) succession of Kutch, northwestern India: Tectonomagmatic implications. *Geosci. Front.* **2018**, *9*, 1883–1902. [[CrossRef](#)]
21. Karsli, O.; Dokuz, A.; Kaliwoda, M.; Uysal, I.; Aydin, F.; Kandemir, R.; Fehr, K.T. Geochemical fingerprints of Late Triassic calc-alkaline lamprophyres from the Eastern Pontides, NE Turkey: A key to understanding lamprophyre formation in a subduction-related environment. *Lithos* **2014**, *196*, 181–197. [[CrossRef](#)]
22. Ma, L.; Jiang, S.Y.; Hou, M.L.; Dai, B.Z.; Jiang, Y.H.; Yang, T.; Zhao, K.D.; Pu, W.; Zhu, Z.Y.; Xu, B. Geochemistry of Early Cretaceous calc-alkaline lamprophyres in the Jiaodong Peninsula: Implication for lithospheric evolution of the eastern North China Craton. *Gondwana Res.* **2014**, *25*, 859–872. [[CrossRef](#)]
23. Tappe, S.; Smart, K.A.; Stracke, A.; Romer, R.L.; Prelević, D.; Bogaard, P.V.D. Melt evolution beneath a rifted craton edge: <sup>40</sup>Ar/<sup>39</sup>Ar geochronology and Sr–Nd–Hf–Pb isotope systematics of primitive alkaline basalts and lamprophyres from the SW Baltic Shield. *Geochim. Cosmochim. Ac.* **2016**, *173*, 1–36. [[CrossRef](#)]
24. Cao, J.; Chen, M.M.; Wan, S.M.; Wang, H.L.; Yi, H.; Lei, H.C. Petrogenesis and Deep Dynamic Processes of Early Permian Alkaline Lamprophyres in the Tarim Large Igneous Province, NW China. *Earth Sci.* **2023**, in press.
25. Chang, Z.G.; Dong, G.C.; Mo, X.X.; Yin, J.; Dong, P.S. Petrogenesis and tectonic implications of the Late Triassic intrusions in the North China Craton: Case study on the Huata complex in the western Yanshan. *Lithos* **2022**, *430*, 106862. [[CrossRef](#)]
26. Hou, Q.; Yang, X.Y.; Tang, J.; Zhou, Q.Z.; Shi, J.B. Geochemistry and geochronology of Early Cretaceous lamprophyres of the Sulu Orogenic Belt: Implications for lithospheric evolution of Eastern China. *Int. Geol. Rev.* **2022**, *65*, 1–17. [[CrossRef](#)]
27. Aghazadeh, M.; Prelević, D.; Badrzadeh, Z.; Braschi, E.; Bogaard, P.V.D.; Conticelli, S. Geochemistry, Sr–Nd–Pb isotopes and geochronology of amphibole- and mica-bearing lamprophyres in northwestern Iran: Implications for mantle wedge heterogeneity in a palaeo-subduction zone. *Lithos* **2015**, *216*, 352–369. [[CrossRef](#)]
28. Xiong, F.H.; Ma, C.Q.; Jiang, H.A.; Liu, B.; Zhang, J.Y.; Zhou, Q.Z. Petrogenetic and tectonic significance of Permian calc-alkaline lamprophyres, East Kunlun orogenic belt, Northern Qinghai-Tibet Plateau. *Int. Geol. Rev.* **2013**, *55*, 1817–1834. [[CrossRef](#)]
29. Xiong, F.H.; Zhong, H.T.; Huang, H.; Liu, X.C.; Hou, M.C. Petrogenetic and tectonic implications of Neoproterozoic igneous rocks from the western Yangtze Block, South China. *Precambrian Res.* **2023**, *387*, 106977. [[CrossRef](#)]
30. Wang, L. The mineralogy, geochemistry and source region of agpaite lamprophyre in Wajilitage, Xinjiang. Master's Thesis, China University of Geosciences, Beijing, China, 2014.
31. Li, C. The Longmucuo-Shuanghu-Lancangjiang plate suture and the north boundary of distribution of Gondwana facies Permo-Carboniferous system in northern Xizang. *China J. Changchun Coll. Geo.* **1987**, *17*, 155–166.
32. Zhai, Q.G.; Jahn, B.; Su, L.; Wang, J.; Mo, X.X.; Lee, H.Y.; Wang, K.L.; Tang, S.H. Triassic arc magmatism in the Qiangtang area, northern Tibet: Zircon U–Pb ages, geochemical and Sr–Nd–Hf isotopic characteristics, and tectonic implications. *J. Asian Earth Sci.* **2013**, *63*, 162–178. [[CrossRef](#)]
33. Kapp, P.; Yin, A.; Manning, C.E.; Murphy, M.; Harrison, T.M.; Spurlin, M.; Ding, L.; Deng, X.G.; Wu, C.M. Blueschist-bearing metamorphic core complexes in the Qiangtang block reveal deep crustal structure of northern Tibet. *Geology* **2000**, *28*, 19–22. [[CrossRef](#)]
34. Pullen, A.; Kapp, P.; Gehrels, G.E.; Vervoort, J.D.; Ding, L. Triassic continental subduction in central Tibet and Mediterranean-style closure of the Paleo-Tethys Ocean. *Geology* **2008**, *36*, 351–354. [[CrossRef](#)]
35. Ding, L.; Kapp, P.; Zhong, D.; Deng, W.M. Cenozoic volcanism in Tibet: Evidence for a transition from oceanic to continental subduction. *J. Petrol.* **2003**, *44*, 1833–1865. [[CrossRef](#)]
36. Liu, J.F.; Chi, X.G.; Zhao, X.Y.; Zhao, Z.; Dong, Y.C.; Li, G.R.; Zhao, Y.D. Chronology, geochemistry and tectonic significances of the Cenozoic Zougouyouchacuo and Nadingcuo volcanic rocks in northern Tibetan Plateau. *Acta. Petrol. Sin.* **2009**, *25*, 3259–3274.
37. Hao, L.L.; Wang, Q.; Kerr, A.C.; Yang, J.-H.; Ma, L.; Qi, Y.; Wang, J.; Ou, Q. Post-collisional crustal thickening and plateau uplift of southern Tibet: Insights from Cenozoic magmatism in the Wuyu area of the eastern Lhasa block. *Geol. Soc. Am. Bull.* **2021**, *133*, 1634–1648. [[CrossRef](#)]
38. Xu, C.B.; Zeng, J.P.; Wang, Q.; Zhang, X.Z.; Ou, Q.; Wang, J.; Hao, L.L.; Chen, Y.W. Eocene adakitic quartz monzonites and granite porphyries from the northern Qiangtang Block, central Tibet: Partial melting of sediment-rich mélange? *Front Earth Sci.* **2022**, *10*, 953448. [[CrossRef](#)]

39. Zong, K.Q.; Klemd, R.; Yuan, Y.; He, Z.Y.; Guo, J.L.; Shi, X.L.; Liu, Y.S.; Hu, Z.C.; Zhang, Z.M. The assembly of Rodinia: The correlation of early Neoproterozoic (ca. 900 Ma) high-grade metamorphism and continental arc formation in the southern Beishan Orogen, southern Central Asian Orogenic Belt (CAOB). *Precambrian Res.* **2017**, *290*, 32–48. [[CrossRef](#)]
40. Wiedenbeck, M.; Alle, P.; Corfu, F.; Griffin, W.L.; Meier, M.; Oberli, F.; Vonquadt, A.; Roddick, J.C.; Spiegel, W. Three natural zircon standards for U-Th-Pb, Lu-Hf, trace-element and REE analyses. *Geostand. Geoanal. Res.* **1995**, *19*, 1–23. [[CrossRef](#)]
41. Liu, Y.S.; Gao, S.; Hu, Z.C.; Gao, C.G.; Zong, K.Q.; Wang, D.B. Continental and oceanic crust recycling-induced melt–peridotite interactions in the Trans-North China Orogen: U-Pb dating, Hf isotopes and trace elements in zircons from mantle xenoliths. *J. Petrol.* **2010**, *51*, 537–571. [[CrossRef](#)]
42. Shan, H.S.; Liu, J.L.; Ding, X.; Chen, X.Y.; Yu, X.Q.; Liu, Z.H.; Xu, Z.Y. Subduction initiation of the Proto-Tethys Ocean that facilitated climate change and biodiversification. *Earth Planet Sc Lett.* **2022**, *600*, 117874. [[CrossRef](#)]
43. Ludwig, K.R. *User's Manual for Isoplot/ex Version 3.00: A Geochronological Toolkit for Microsoft Excel*; Special Publication; Berkeley Geochronology Center: Berkeley, CA, USA, 2003.
44. Hu, Z.C.; Liu, Y.S.; Gao, S.; Liu, W.G.; Zhang, W.; Tong, X.R.; Lin, L.; Zong, K.Q.; Li, M.; Chen, H.H.; et al. Improved in situ Hf isotope ratio analysis of zircon using newly designed X skimmer cone and jet sample cone in combination with the addition of nitrogen by laser ablation multiple collector ICP-MS. *J. Anal. Atom. Spectrom.* **2012**, *27*, 1391–1399. [[CrossRef](#)]
45. Le, M.R.W.; Bateman, P.; Dudek, A.; Keller, J.; Lameyre, J.; Le, B.M.J.; Sabine, P.A.; Schmid, R.; Sorensen, H.; Streckeisen, A. *A classification of igneous rocks and glossary of terms. Recommendations of the IUGS Subcommittee on the Systematics of Igneous rocks*, 1st ed.; Blackwell: Oxford, UK, 1989; pp. 130–171.
46. Middlemost, E.A.K. Naming materials in the magma/igneous rock system. *Earth. Sci. Rev.* **1994**, *37*, 215–224. [[CrossRef](#)]
47. Rock, N.M.S. The Nature and Origin of Lamprophyres: An Overview. In *Magmatism in the Ocean Basins*; Special Publications; Saunders, A.D., Norry, M.J., Eds.; Geological Society: London, UK, 1987; Volume 30, pp. 191–226.
48. Sun, S.S.; McDonough, W.F. Chemical and isotopic systematics of oceanic basalts: Implications for mantle composition and processes. In *Magmatism in the Ocean Basins*; Special Publications; Saunders, A.D., Norry, M.J., Eds.; Geological Society: London, UK, 1989; Volume 42, pp. 313–345.
49. Niu, Y.L.; Gilmore, T.; Mackie, S.; Greig, A.; Bach, W. Mineral chemistry, whole-rock compositions, and petrogenesis of Leg 176 gabbros: Data and discussion. In *Proceedings of the Ocean Drilling Program, Scientific Results*; Ocean Drilling Program: College Station, TX, USA, 2002.
50. Niu, Y.L.; Regelous, M.; Wendt, I.J.; Batiza, R.; O'hara, M.J. Geochemistry of near-EPR seamounts: Importance of source vs. process and the origin of enriched mantle component. *Earth. Planet. Sci. Lett.* **2002**, *199*, 327–345. [[CrossRef](#)]
51. Kelemen, P.B.; Hanghøj, K.; Greene, A.R. One view of the geochemistry of subduction-related magmatic arcs, with an emphasis on primitive andesite and lower crust. In *Treatise on Geochemistry*; Holland, H.D., Turekian, K.K., Eds.; Elsevier: Amsterdam, Netherlands, 2007; Volume 3, pp. 1–70.
52. Lai, S.C.; Qin, J.F.; Li, Y.F.; Long, P. Geochemistry and petrogenesis of the alkaline and calc-alkaline series Cenozoic volcanic rocks from Huochetou mountain, Tibetan plateau. *Acta. Petrol. Sin.* **2007**, *23*, 709–718.
53. Wu, F.Y.; Yang, Y.H.; Xie, L.W.; Yang, J.H.; Xu, P. Hf isotopic compositions of the standard zircons and baddeleyites used in U-Pb geochronology. *Chem. Geol.* **2006**, *234*, 105–126. [[CrossRef](#)]
54. Lu, Y.J.; Kerrich, R.; Mccuaig, T.C.; Li, Z.X.; Hart, C.J.R.; Cawood, P.A.; Hou, Z.Q.; Bagas, L.; Cliff, J.; Belousova, E.A.; et al. Geochemical, Sr-Nd-Pb, and Zircon Hf-O Isotopic Compositions of Eocene-Oligocene Shoshonitic and Potassic Adakite-like Felsic Intrusions in Western Yunnan, SW China: Petrogenesis and Tectonic Implications. *J. Petrol.* **2013**, *54*, 1309–1348. [[CrossRef](#)]
55. Liu, J.H.; Gou, G.N.; Wang, Q.; Zhang, X.Z.; Guo, H.F. Petrogenesis of Eocene high-silica granites in the Maliaoshan area, northern Tibet: Implications for the Eocene magmatic flare-up in the Northern Qiangtang Block. *J. Asian. Earth. Sci.* **2022**, *234*, 105268. [[CrossRef](#)]
56. Qian, Y.; Tian, S.N.; Li, Y.J.; Sun, F.Y.G. Zircon U-Pb age and geochemical constraints on the origin and tectonic implication of the Tuotuohe Cenozoic alkaline magmatism in Qinghai–Tibet Plateau. *Acta Geochim.* **2020**, *39*, 67–84. [[CrossRef](#)]
57. Zeng, Y.C.; Xu, J.F.; Li, M.J.; Chen, J.L.; Wang, B.D.; Huang, F.; Ren, S.H. Late Eocene two-pyroxene trachydacites from the southern Qiangtang Terrane, central Tibetan Plateau: High-temperature melting of overthickened and dehydrated lower crust. *J. Petrol.* **2021**, *62*, egab080. [[CrossRef](#)]
58. Zhao, Z.; Chi, X.G.; Liu, J.F.; Li, G.R.; Zhao, Y.D. Geochemical feature and its tectonic significance of Gemucuo Oligocene potassic volcanic rocks in the Qiangtang area, Tibet, China. *Geol. Bull. China* **2009**, *28*, 463–473.
59. Liu, S.; Hu, R.Z.; Chi, X.G.; Li, C.; Feng, C.X.; Wang, T.W. Post-collisional ultrapotassic volcanic rocks in Qiangtang rock belt. *Geotec. Metallo.* **2003**, *27*, 167–175.
60. Qin, Z.P.; Du, Q.D.; Zhang, G.Y.; Duo, J.; Li, M.; Huang, C. Origin and tectonic significance of Eocene sodic lamprophyres in the Southern Qiangtang Orogen, Tibet. *J. Asian Earth Sci.* **2023**, *250*, 105629. [[CrossRef](#)]
61. Liu, D.L.; Shi, R.D.; Ding, L.; Huang, Q.S.; Zhang, X.R.; Yue, Y.H.; Zhang, L.Y. Zircon U-Pb age and Hf isotopic compositions of Mesozoic granitoids in southern Qiangtang, Tibet: Implications for the subduction of the Bangong–Nujiang Tethyan Ocean. *Gondwana Res.* **2017**, *41*, 157–172. [[CrossRef](#)]
62. Rudnick, R.; Gao, S. Composition of the continental crust. In *Treatise on Geochemistry*; Holland, H.D., Turekian, K.K., Eds.; Elsevier-Pergamon: Oxford, UK, 2003; Volume 3, pp. 1–64.

63. Nicholls, I.A.; Harris, K.L. Experimental rare earth element partition coefficients for garnet, clinopyroxene and amphibole coexisting with andesitic and basaltic liquids. *Geochim. Cosmochim. Acta* **1980**, *44*, 287–308. [[CrossRef](#)]
64. Foley, S.F.; Jackson, S.E.; Fryer, B.J.; Greenough, J.D.; Jenner, G.A. Trace element partition coefficients for clinopyroxene and phlogopite in an alkaline lamprophyre from Newfoundland by LAM-ICP-MS. *Geochim. Cosmochim. Acta* **1996**, *60*, 629–638. [[CrossRef](#)]
65. Latourrette, T.; Hervig, R.L.; Holloway, J.R. Trace element partitioning between amphibole, phlogopite, and basanite melt. *Earth Planet. Sci. Lett.* **1995**, *135*, 13–30. [[CrossRef](#)]
66. Adam, J.; Green, T.H.; Sie, S.H. Proton microprobe determined partitioning of Rb, Sr, Ba, Y, Zr, Nb and Ta between experimentally produced amphiboles and silicate melts with variable F content. *Chem. Geol.* **1993**, *109*, 29–49. [[CrossRef](#)]
67. Ma, L.; Jiang, S.Y.; Hofmann, A.W.; Dai, B.Z.; Hou, M.L.; Zhao, K.D.; Chen, L.H.; Li, J.W.; Jiang, Y.H. Lithospheric and asthenospheric sources of lamprophyres in the Jiaodong Peninsula: A consequence of rapid lithospheric thinning beneath the North China Craton? *Geochim. Cosmochim. Acta* **2014**, *124*, 250–271. [[CrossRef](#)]
68. Furman, T.; Graham, D. Erosion of lithospheric mantle beneath the East African Rift system: Geochemical evidence from the Kivu volcanic province. In *Developments in Geotectonics*; Elsevier: Amsterdam, Netherlands, 1999; Volume 24, pp. 237–262.
69. Wang, K.; Plank, T.; Walker, J.D.; Smith, E.I. A mantle melting profile across the Basin and Range, SW USA. *J. Geophys. Res. Sol. Earth.* **2002**, *107*, ECV 5-1–ECV 5-21. [[CrossRef](#)]
70. Wang, C.; Liu, H.; Feng, H.B.; Deng, J.H.; Liu, X.F.; Zhao, F.F. Geochemistry and U-Pb ages of the diabases from the Luoji area, western Yunnan, China: Implications for the timing of initial rifting of the Ganzi-Litang Ocean. *Geol. Croat.* **2019**, *72*, 19–32. [[CrossRef](#)]
71. Ning, W.K.; Chi, X.G.; Liu, J.F.; Zhao, Z.; Li, C. Genesis of Heishibeihu Cenozoic potassic volcanic rocks from northern Qinghai-Tibet Plateau China. *Geol. Bull. China* **2009**, *28*, 1355–1360.
72. Pearce, J.A. Geochemical fingerprinting of oceanic basalts with applications to ophiolite classification and the search for Archean oceanic crust. *Lithos* **2008**, *100*, 14–48. [[CrossRef](#)]
73. Class, C.; Miller, D.M.; Goldstein, S.L.; Langmuir, C.H. Distinguishing melt and fluid subduction components in Umnak Volcanics, Aleutian Arc. *Geochem. Geophys. Geosy.* **2000**, *1*. [[CrossRef](#)]
74. Castillo, P.R.; Rigby, S.J.; Solidum, R.U. Origin of high field strength element enrichment in volcanic arcs: Geochemical evidence from the Sulu Arc, southern Philippines. *Lithos* **2007**, *97*, 271–288. [[CrossRef](#)]
75. Castillo, P.; Newhall, C. Geochemical constraints on possible subduction components in lavas of Mayon and Taal volcanoes, southern Luzon, Philippines. *J. Petrol.* **2004**, *45*, 1089–1108. [[CrossRef](#)]
76. Hermann, J.; Green, D.H. Experimental constraints on high pressure melting in subducted crust. *Earth. Planet. Sci. Lett.* **2001**, *188*, 149–168. [[CrossRef](#)]
77. Pearce, J.A. Trace element characteristics of lavas from destructive plate boundaries. In *Andesites: Orogenic Andesites and Related Rocks*; Thorpe, R.S., Ed.; Wiley: Hoboken, NJ, USA, 1982; pp. 528–548.
78. Zhao, Z.D.; Mo, X.X.; Dilek, Y.; Niu, Y.L.; Depaolo, D.J.; Robinson, P.; Zhu, D.C.; Sun, C.G.; Dong, G.C.; Zhou, S. Geochemical and Sr–Nd–Pb–O isotopic compositions of the post-collisional ultrapotassic magmatism in SW Tibet: Petrogenesis and implications for India intra-continental subduction beneath southern Tibet. *Lithos* **2009**, *113*, 190–212. [[CrossRef](#)]
79. He, X.; Wang, W.; Santosh, M.; Yao, J.C.; Gao, K.T.; Zhang, Y.H.; Lu, D.G.; Guo, L.S. Late Neoproterozoic crustal growth under paired continental arc-back arc system in the North China Craton. *Geosci. Front.* **2021**, *12*, 101120. [[CrossRef](#)]
80. Guo, Z.F.; Wilson, M.; Zhang, M.L.; Cheng, Z.H.; Zhang, L.H. Post-collisional ultrapotassic mafic magmatism in South Tibet: Products of partial melting of pyroxenite in the mantle wedge induced by roll-back and delamination of the subducted Indian continental lithosphere slab. *J. Petrol.* **2015**, *56*, 1365–1406. [[CrossRef](#)]
81. Chakrabarti, R.; Basu, A.R.; Santo, A.P.; Tedesco, D.; Vaselli, O. Isotopic and geochemical evidence for a heterogeneous mantle plume origin of the Virunga volcanics, Western rift, East African Rift system. *Chem. Geol.* **2009**, *259*, 273–289. [[CrossRef](#)]
82. Wang, Q.; Wyman, D.A.; Li, Z.X.; Sun, W.D.; Chung, S.L.; Vasconcelos, P.M.; Zhang, Q.Y.; Dong, H.; Yu, Y.S.; Pearson, N. Eocene north–south trending dikes in central Tibet: New constraints on the timing of east–west extension with implications for early plateau uplift? *Earth Planet. Sci. Lett.* **2010**, *298*, 205–216. [[CrossRef](#)]
83. Pan, G.T.; Wang, P.S.; Xu, Y.R. *Cenozoic Tectonic Evolution of Qinghai-Tibet Plateau*; Geology Press: Beijing, China, 1990; pp. 1–190.
84. Wang, Q.; Wyman, D.A.; Xu, J.F.; Dong, Y.H.; Vasconcelos, P.M.; Pearson, N.; Wan, Y.S.; Dong, H.; Li, C.F.; Yu, Y.S.; et al. Eocene melting of subducting continental crust and early uplifting of central Tibet: Evidence from central-western Qiangtang high-K calc-alkaline andesites, dacites and rhyolites. *Earth Planet. Sci. Lett.* **2008**, *272*, 158–171. [[CrossRef](#)]
85. Ou, Q.; Wang, Q.; Wyman, D.A.; Zhang, H.X.; Yang, J.H.; Zeng, J.P.; Hao, L.L.; Chen, Y.W.; Liang, H.; Qi, Y. Eocene adakitic porphyries in the central-northern Qiangtang Block, central Tibet: Partial melting of thickened lower crust and implications for initial surface uplifting of the plateau. *J. Geophys. Res. Sol. Earth* **2017**, *122*, 1025–1053. [[CrossRef](#)]
86. Zhang, R. Volcanic Rocks from Qiangtang, Northern Tibet Petrogenesis of the Cenozoic Alkaline Potassic-Ultrapotassic. Ph.D. Thesis, Jilin University, Changchun, China, 2018.

**Disclaimer/Publisher’s Note:** The statements, opinions and data contained in all publications are solely those of the individual author(s) and contributor(s) and not of MDPI and/or the editor(s). MDPI and/or the editor(s) disclaim responsibility for any injury to people or property resulting from any ideas, methods, instructions or products referred to in the content.